Comparison of Power Law Tropospheric Correction for Time Series InSAR Application

NOORLAILA H. ISYA[1 2], ANIKA RIEDEL[1], BJÖRN RIEDEL[1] & WOLFGANG NIEMEIER[1]

Abstract: Radar interferometric technology is nowadays considered as one geodetic method to observe earth surface changes. The use of time series analysis in SAR imageries could figure out slow periodical displacement rates on natural hazard phenomena such as mass movement in landslide prone areas and crustal deformation in tectonic areas. However, this multi-temporal SAR results could be biased due to effect of atmospheric phase screen (APS) when microwave signals are going through tropospheric layer. Power law tropospheric correction is a method that recently used on InSAR application to minimize atmospheric noise both spatially and temporally. The method attempts to find a correlation of phase delay to hydrostatic and wet components in troposphere properties. Thus, we try to estimate the tropospheric delay on individual interferograms and apply Small Baseline Subset (SBAS) on InSAR in different regions. The case study of a small region is represented in Ciloto, West Java, Indonesia and for a large region, we chose an area located at northern Baja California, Ensenada, Mexico. 50 Sentinel-1A ascending SAR Imageries have been proceed in Ciloto Landslide prone area from October 2014 to September 2017. In term of detecting the deformation signal at Baja California, we tested 44 Envisat Descending data from February 2003 to October 2010. Sounding data are needed to calculate tropospheric delay at different altitudes. They are taken from International Upper Air network data which provide variables of atmospheric pressure, temperature and relative humidity. We find the estimation of phase delay using topography correlated by a power law and reference height could improve the displacement's accuracy value. Nevertheless, the attention either under or over estimation due to band-filtering performance and correlated height terrain should be watched out for every interferogram. We then conduct general assessment before and after power law tropospheric correction for small baseline InSAR results and compare them to measurements from Extensometer installed in Ciloto. For the large area in northern Baja California, Mexico, the phase-based power law correction is compared to atmospheric delay maps generated by MERIS, a spectrometer instrument on board Envisat, in condition to free cloud cover 50% and 90% at the study area.

1 Introduction

Interferometry Synthetic Aperture Radar is one promising techniques to measure the earth surface changes on space borne. A considerable number of research studies research have identified seismic activities such as earthquake 's impact (FUNNING et al. 2005), subsidence due to over-exploitation of ground water (CHEN et al. 2016) and oilfields (LIU et al. 2015), the behaviour of volcanoes (HOOPER et al. 2007), and slow movement in landslide prone areas (CASCINI et al. 2010). Permanent Scatter (PS) (FERRETTI et al. 2001) and SBAS techniques

[1] Technische Universität Braunschweig, Bienroder Weg 81, D- 38106 Braunschweig, E-Mail: n.isya@tu-bs.de
[2] Institut Teknologi Sepuluh Nopember, Jl. Raya ITS – 60111 Surabaya, Indonesia

(BERARDINO et al. 2002) are advance InSAR methods to generate real deformation and reduce unwanted signals coming from orbit and topographic errors, atmospheric effects, and noises. Some spatial correlated terms, orbit to height errors, could be removed from interferogram considering to the use of abundant SAR imageries and finding out the stable scatters. Previously, atmospheric terms could be filtered out as well when we consider that atmospheric signals are random in time (e.g., FERRETTI et al. 2001; BERARDINO et al. 2002). However, a recent study proved that they are also temporally correlated to stratified tropospheric delays (DOIN et al. 2009). Thus, removing the atmospheric phase screen especially for tropospheric delay patterns using low-pass filtering might be miss interpretation of certain deformation signals as a noise or otherwise. If we observe some high level deformations of large scale unit (cm to m) at relative small area, we could neglect the effect of atmospheric phase screen due to the same of phase characteristics between pixels. Nevertheless, the monitors of crustal deformation, subsidence and slope movement could be considered as a very low rate displacement (mm to cm) whose InSAR practicals have to pay attention to atmospheric artifacts performing more accurate results of displacements.

Two atmospheric layers which mostly effect microwave signals are propagating through ionosphere and troposphere. Ionospheric delay mostly finds on L band sensor, ALOS PALSAR, and will be neglected on the processing procedure. The focus study is correcting the tropospheric delay using power law function (BEKAERT et al. 2015) on InSAR process and how the correction impacts the results of displacement value both in Indonesia and Mexico areas. For the Indonesia case, we observe slow movement in Ciloto, West Java, where the area has a high risk of landslide hazard using 50 SAR images of Sentinel 1A ascending orbit. Furthermore, we attempt to detect crustal deformation near to Agua Blanca Fault and additionally a subsidence around agriculture area in Manaedero Valley using 44 images of Envisat descending orbit.

2 Study Areas and Method

The troposphere delay correction will be tested on two case studies, which are Ciloto, Indonesia and Baja California, Mexico. Both of those are located on the mountainous terrain where probably having high precipitation on the top terrain so that it may has a different troposphere propagation signal between the flat and hilly area. Hence, these delay variations could cause miss interpretation of interferograms (GOLDSTEIN1995). HANSSEN (2001) distinguish two types of atmospheric signal based on their physical origin. The first one, turbulent mixing, is caused by turbulent process in the atmosphere. Turbulent delay could affects both flat and mountain terrain. It makes phase artifacts on the interferogram due to spatial heterogeneity in the refractivity. Secondly, vertical stratification is mostly correlated to topography and only affects mountainous terrain (MASSONET & FEIGL 1998). It is caused by different vertical refractivity profiles between master-slave SAR acquisitions considered as no heterogeneities within the horizontal layers.

Estimation of tropospheric delay might be described with a mathematical model which is generally divided as systematic and stochastic component. Figure 1 explains shortly the scheme of atmospheric delay that most recent atmospheric studies categorizing the delay estimation.

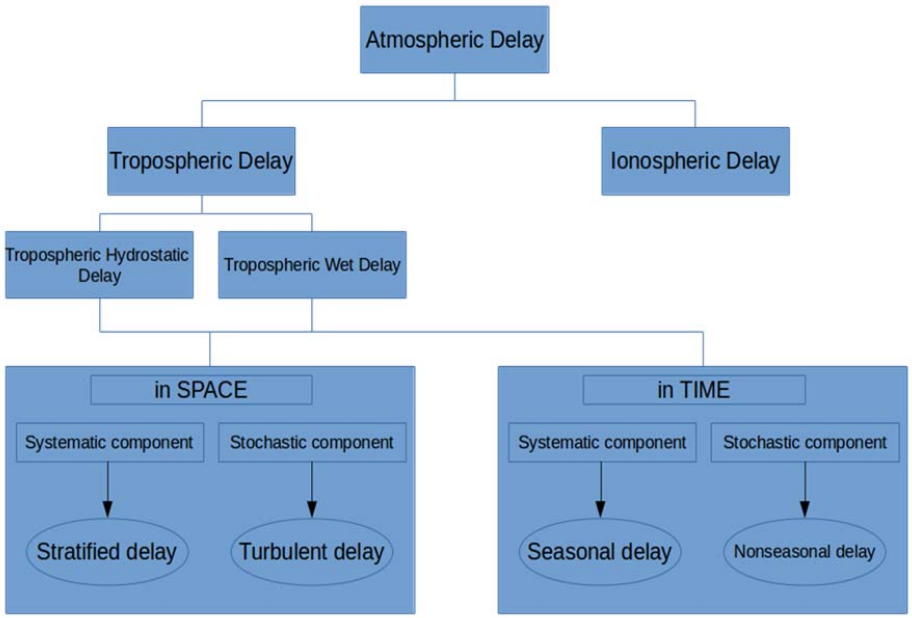

Fig. 1: The scheme of atmospheric delay that might influence interpretation between SAR acqusitions

According to the troposphere layer, it contains of hydrostatic delay and wet delay. The determined parameters of hydrostatic delay are the refractivity from dry air (atmospheric pressures and temperature) and of wet delay from wet air (partial pressure of water vapor and temperature). SMITH & WEINTRAUB (1953) characterized the phase delay through atmosphere using the refractivity (N), with

$$N = \left(k_1 \frac{P}{T}\right)_{hydro} + \left(k'_2 \frac{e}{T} + k_3 \frac{e}{T^2}\right)_{wet} \tag{1}$$

where P = total atmospheric pressure, T = temperature and e = partial pressure of water pavor, k1, k'2, k3 are constants parameter with 77.6 K hPa-1, 23.3 K hPa-1 and 3.75.105 K2 hPa-1, respectively (THAYER 1974). Furthermore, if we consider tropospheric phase delay (ϕtropo) between pixels (p,q) and SAR acquisitions along radar line of sight (HANSSEN 2001), it can be defined as

$$d_{tropo} = 10^{-6}(\cos\theta)^{-1}\left[\int_{h_p}^{h_{top,p}} N(h)\,dh - \int_{h_q}^{h_{top,q}} N(h)\,dh\right] \tag{2}$$

$$\phi_{tropo} = \frac{-4\pi}{\lambda}\, d_{tropo} \tag{3}$$

where d_{tropo} = the tropospheric (slant) delay, θ = the incidence angle, λ = the radar wavelength and h = height coresponds to the integration of the refractivity between h and the top of the troposphere (h_{top}).

Several main approaches to estimate tropospheric delay have been conducted to correct InSAR results (Figure 2). Three main source model are based on numerical weather model, for instance,

(i) high spatial and temporal resolution weather forecast models (WRF) (JUNG et al. 2014), (ii) global atmospheric reanalysis models with low spatial and temporal resolution ERA-1 (~80 km), MERRA2 (~ 55 km) from the European Centre for Medium-Range Weather Forecasts, and (iii) Generic Atmospheric Correction Online Service for InSAR (YU et al. 2018). The second one is from satellite spectrometers, which use observations of atmospheric water vapor from Moderate Resolution Imaging Spectroraidometer (MODIS) and Medium-Resolution Imaging Spectrometer on board Envisat (MERIS) (LI et al. 2009). Another strategy is using a phase based model itself with main purpose to reduce stratified delay correlated with topography variations. A former method of phase based use linear relation between tropospheric phase delay and topography and recently improved by using a spatially variable power law approach (BEKAERT et al. 2015). On this article, we assess only a power law method and test the tropospheric correction at small area in Ciloto and large area in northern Baja California.

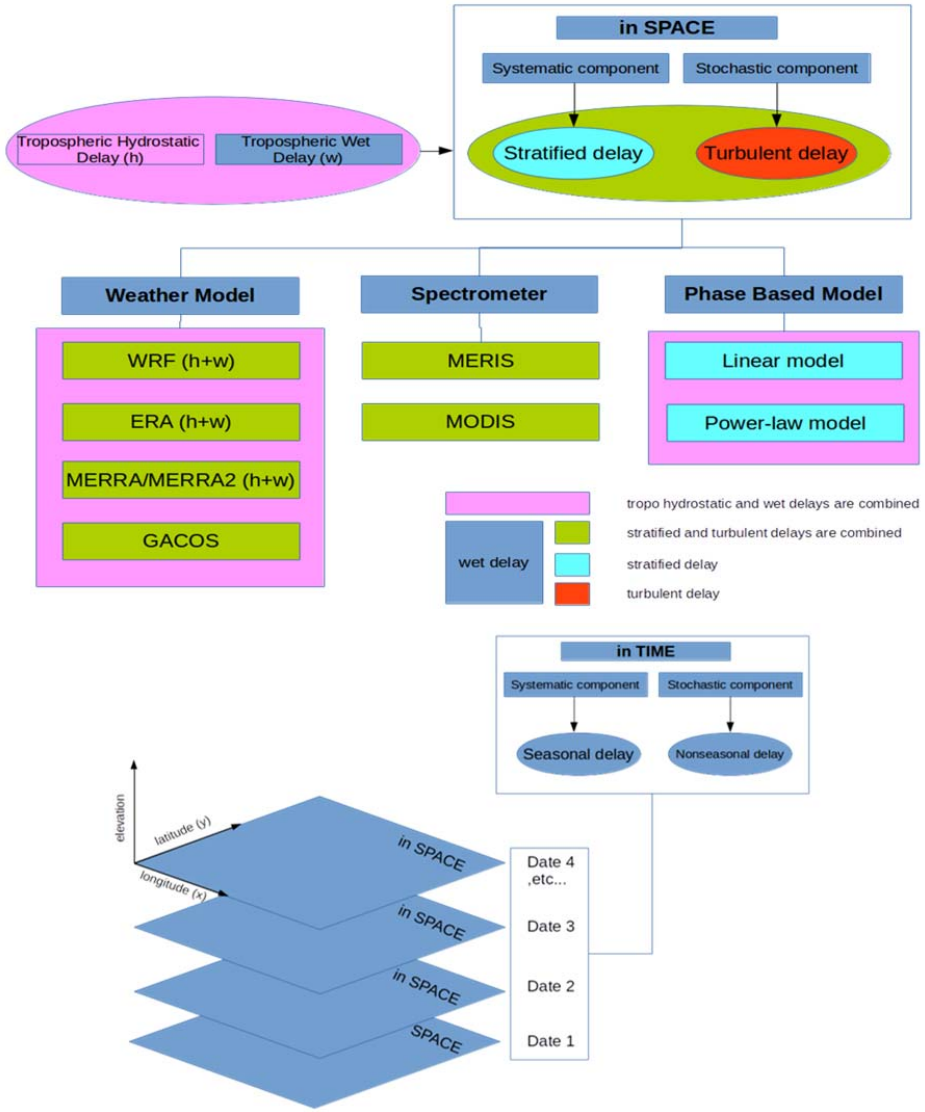

Fig. 2: Different source and strategies for estimating tropospheric delay in space (top) and in time (bottom)

2.1 Ciloto, West Java, Indonesia

Ciloto is located on a hilly ridge to creek valley southern of Cijember River (Figure 3). This area has been built for residence, tourism (Puncak) and agriculture. The main type of rock around Ciloto is Quaternary volcanic rocks consisting of basalt, andesitic tuffs especially breccia, and lava from local vents. In recent years, many evidences for ground displacements have been occurred in Ciloto. Starting from the top of valley's body, ground movements were about 1-2 m located at a resort hotel reported in 2014. The swimming pool of the hotel could not be operated any more since the incident. In the same year, 200 m away to first evidence, 33 families were evacuated from their houses since cracks have been found on several house's walls. Moreover, there was also a total broken house due to miss construction and easily triggered by the ground movements. Therefore, Technical Research Center for Geological Hazard (BPPTKG) has installed extensometer near to the resort hotel since 2014 because of the phenomenon. On next section, we compare the LOS displacement from time series InSAR to graphic displacements from extensometer in the same time overlap.

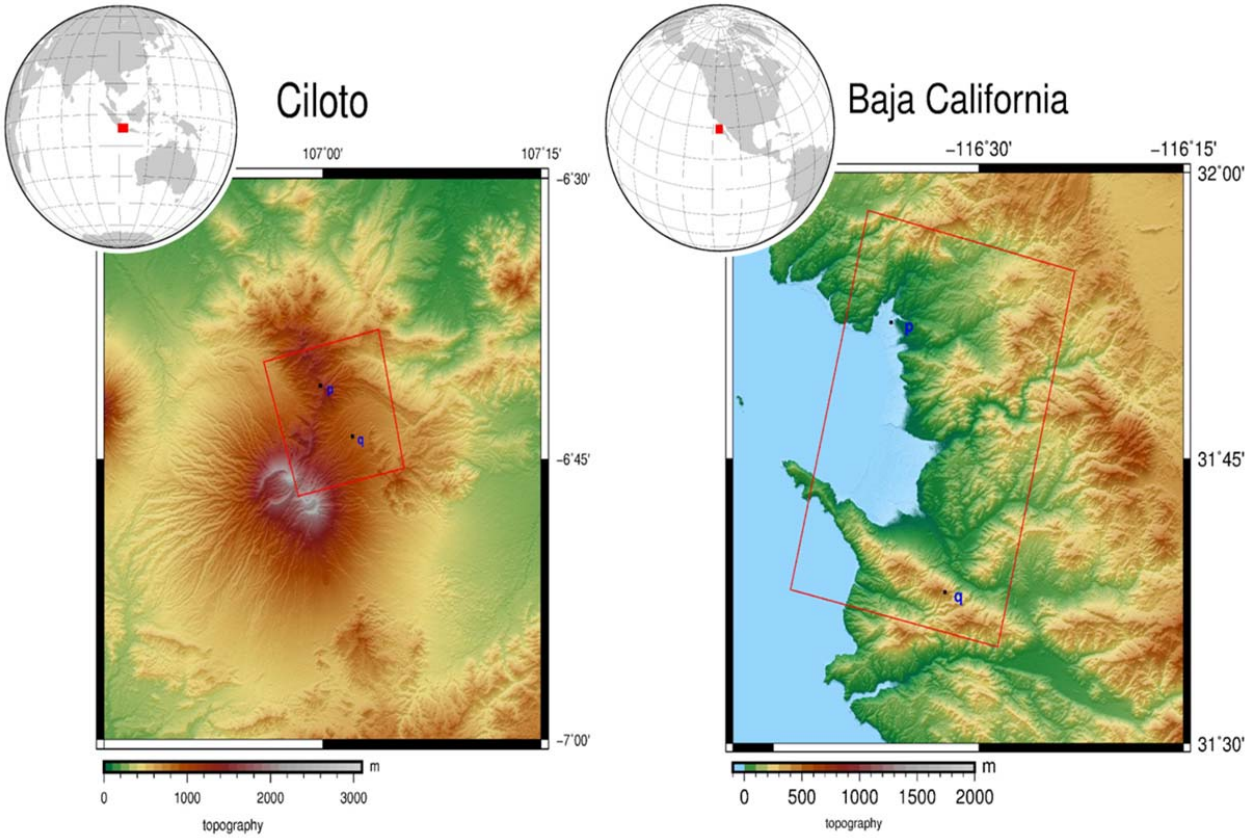

Fig. 3: Study areas: (left) Ciloto, West Java, Indonesia with the red rectangle line showing Sentinel-1A ascending scene borders (Long E:105.5° – 108.5° and Lat S: -5.5° - 7.5°) and (right) Northern Baja California, Ensenada, Mexico with the red rectangle line showing Envisat descending scene borders (Long W: 117.5° – 115.5° and Lat N: 30.5° – 32.5°). Pixel p and q refer to different phase delays showed on Fig. 4 and Fig. 5.

Furthermore, several landslides occurred at Puncak highway, the middle part of study area. *Indonesian National Board for Disaster Management* (BNPB) recorded two big landslide

hazards in Bandung and Bandung Barat, West Java at 23th February 2010 and 25th March 2013 with 33 died, 17 were injured, 936 lost their houses and 14 died, 23 were injured and 185 lost their houses, respectively. Even two landslides periodically were occurred on the same location, Raya Puncak Highway at Km.81, close to Bumi Aki restaurant. The first mass movement was in 2015 placed next to the body of Raya Puncak highway and damaged the local infrastructure and plant field around the area. The second event happened in rainy season, February 2017. This hazard belongs to a small type of mass wasting which the impact area was only ± 25 x 25 m. However, the deposit debris flow right into Raya Puncak highway and disconnected one of the most important access pathways between Bogor and Bandung city.

In general the effect of atmospheric phase screen is visible mostly in large area, such as, crustal deformation monitoring. However, Ciloto is placed on mountainous terrain and has high relative humidity. We demonstrate the temporal variation of the hydrostatic delay and wet delay between two pixel p [106.9976° ; -6.6851°] located on a hilly area and pixel q [107.0343° ; -6.7299°] located on a flat area. The length between the two pixels is about 6.5 km and 380 m elevation differences. Since the SAR scene was cropped to the small coverage to evaluate only at the prone landslide region, we do not attempt to figure out the behavior of tropospheric phase delay in such large area.

The temporal variation of hydrostatic and wet delay is calculated during the Sentinel 1A SAR acquisitions from October 2014 – September 2017 at 11:00 – 12:00 hour using weather model from ERA-1 Interim. Figure 4 describes the effect of slant hydrostatic delay (SHD) and slant wet delay (SWD) between these two pixels. The seasonal component is assumed to a periodic signals described as Fourier series model, a summation of sine and cosine functions with annual and biannual components (FATTAHI et al. 2015) using the following function

$$\text{SHD or SWD} = a_o + \sum_{i=1}^{2} a_i \cos(2\pi i t) + b_i \sin(2\pi i t) \tag{4}$$

$$\text{STD} = \text{SHD} + \text{SWD} \tag{5}$$

where a_o = intercept, a_1,b_1 = the coefficients of annual components, a_2,b_2 = the coefficients of semi-annual components, t = period (every day in SAR acquisitions' duration) and STD = Slant Total Delay. We assume the stochastic components of time series of relative delay are residual of ERA-1 and best fitted seasonal. The relative delay and seasonal component could be plotted as Gaussian distribution in which the standard deviations of SHD, SWD, SHD are 0.0342, 0.4545, 0.4438, respectively. The highest and lowest peak of SHD is -14.6630 cm and -14.4246 cm, for SWD is -6.6920 cm and -3.7747 cm, respectively. The interval delay for SHD and SWD is 0.2385 cm and 2.9173 cm for 3 years. Hence, we could find out the interval between highest and lowest peak of STD about 2.9659 cm.

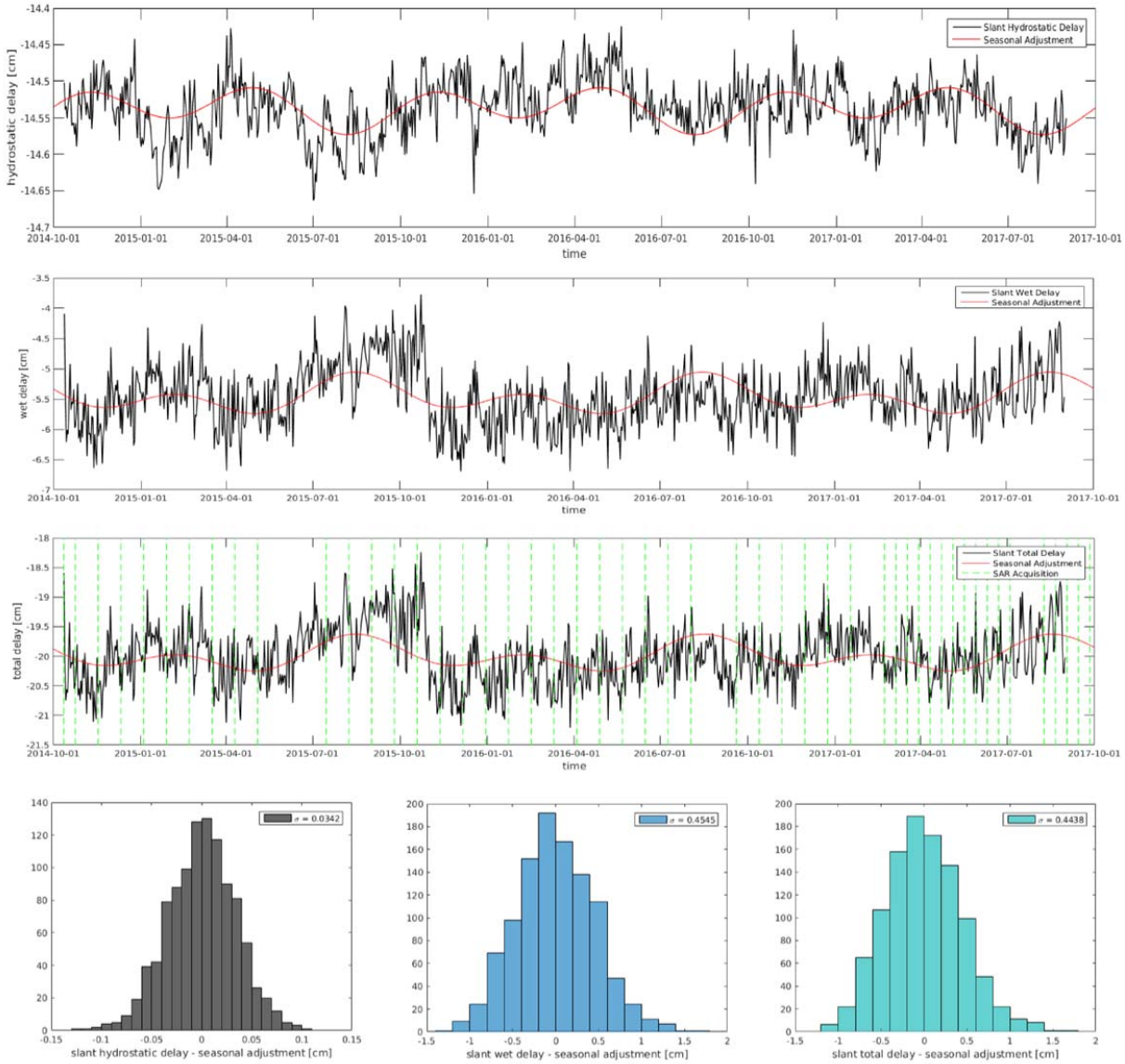

Fig. 4: (The top rows) Time series of relative slant hydrostatic delay (top), slant wet delay (middle) and slant total delay (below) from ERA-1 with seasonal model for each delay between pixels [p,q] in Ciloto region. The green line is Sentinel-1A date acquisitions. (The bottom row) Non-seasonal component with Gaussian distribution.

2.2 Northern Baja California, Ensenada, Mexico

The other second study area is located in an arid coastal region in the northern part of the Peninsula of Baja California, 110 km south from the US-México border line (Figure 3). The region is morphologically characterized by coastal and alluvial flatlands, where the city of Ensenada and the croplands of Maneadero are located. These flatlands are surrounded by the Guadalupe and Ojos Negros intermountain valleys. The Agua Blanca fault is the southern border of our study area and extends from NW to SE as a 120 km length of dextral strike-slip fault. The geological background of this area was explained more at previous works (DIXON et al. 2002; ANIKA et al. 2018).

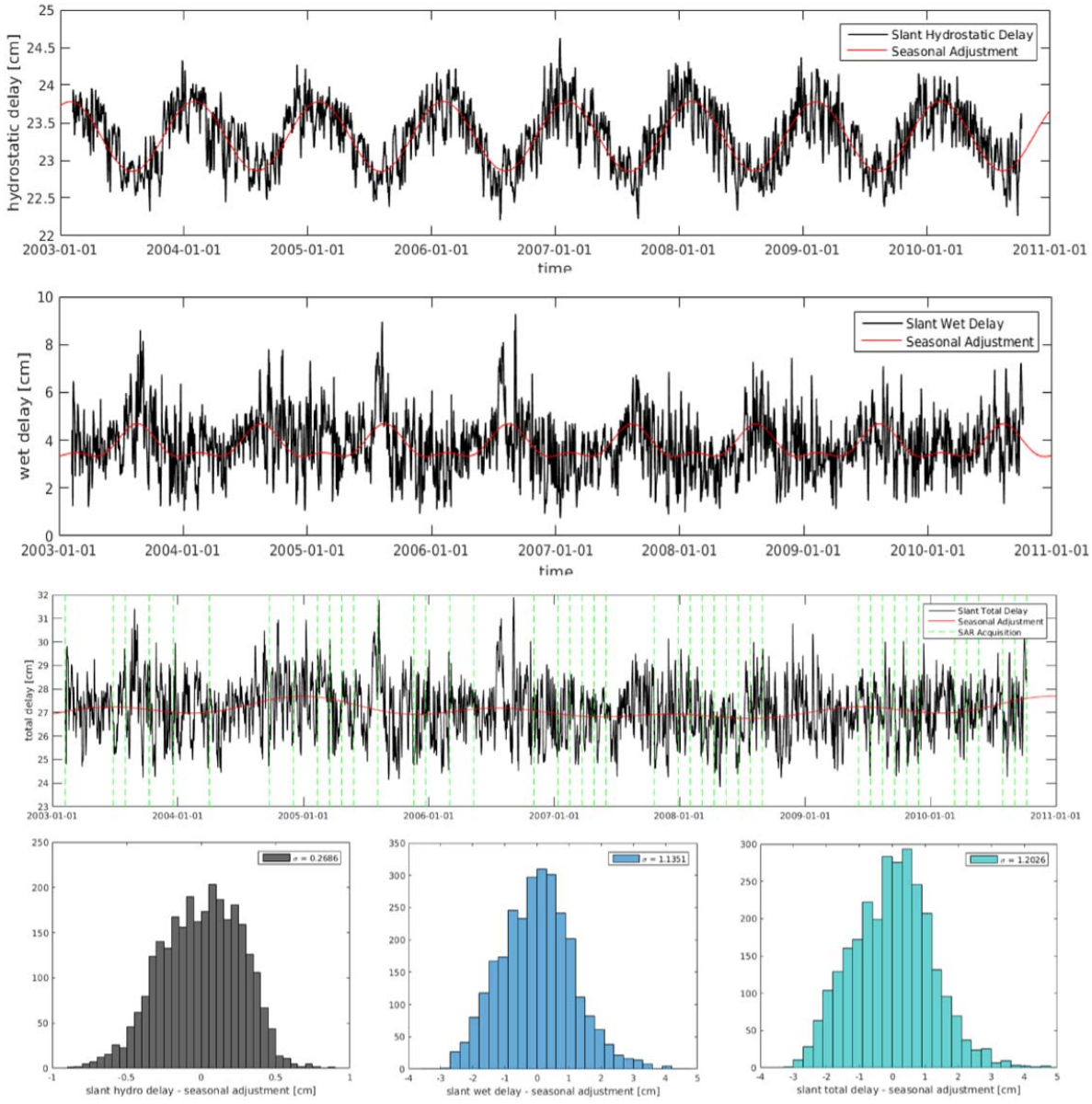

Fig. 5: (The top rows) Time series of relative slant hydrostatic delay (top), slant wet delay (middle) and slant total delay (below) from ERA-1 with seasonal model for each delay between pixels [p,q] in Ensenada region. The green line is Envisat date acquisitions. (The bottom row) Non-seasonal component with Gaussian distribution.

Northern Baja California has a big possibility to observe earth's surface change, for example, crustal deformation due to tectonic activity and subsidence due to over-exploitation through water pumping in agricultural areas like in Maneadero Valley. The region has various terrains from flats in El Bajio and Maneadero Valley to mountainous on Punta Banda Ridge. Therefore, atmospheric phase screen could affect microwave propagating signal especially through tropospheric layers in this region and make a dominant stratified delay in the interferogram.

As the section 2.1, we demonstrate also the temporal variation of the hydrostatic delay and wet delay between two pixel *p* [-116.6069°; 31.8690°] located on flat terrain and pixel *q* [-116.5410 °; 31.6327 °] located on mountainous terrain. The height difference between pixels is 910 m with

29 km length. The calculation of seasonal and non-seasonal delay is the same as what we applied in Ciloto region. The relative delay and seasonal component could be plotted as Gaussian distribution in which the standard deviations of SHD,SWD,SHD are 0.2686, 1.1351, 1.2026, respectively. The highest and lowest peak of SHD is 22.2033 cm and 24.6427 cm, for SWD is 0.7407 cm and 9.2680 cm, respectively. The interval delay for SHD and SWD is 2.4214 cm and 8.5274 cm for 8 years. Hence, we could find out the interval between highest and lowest peak of STD about 8.0610 cm. According to Figure 5, the seasonal model with the same summation of sine and cosine functions is not best fitted to STD since the periodic harmony between SHD and SWD in Ensenada is quite different and clearly shows a greater range interval delay (8.06 cm) than its in Ciloto (2.96 cm). The high peak of seasonal delay for SHD is occurred on every October-November annually. On the other hand, SWD has high peak of it on every January - March annually.

2.3 InSAR Processing

We generate the interfrograms using GMTSAR (SANDWELL et al. 2011) for Sentinel-1A imageries in Ciloto, Indonesia and DORIS (KAMPES et al. 2003) for Envisat imageries in Ensenada, Mexico. Furthermore, we select Persistent Scatter (PS) candidates with Slowly Decorellating Filter Phase (SDFP) algorithm. They are processed by StaMPS, a non-commercial statistical InSAR software, developed by HOOPER (2012). All interferograms are selected by small temporal and perpendicular baseline parameters. We choose master-slave pairs with baseline less than 150 days; 150 m in Ciloto and 365 days; 500 m in Ensenada adding additional pairs to make sure there is no isolated network. The final small baseline configuration could be seen on Figure 6 and StaMPS processing parameters both in study areas are described in Table 1. Additionally, the phase contribution due to oscillator drift is also removed in Envisat processing.

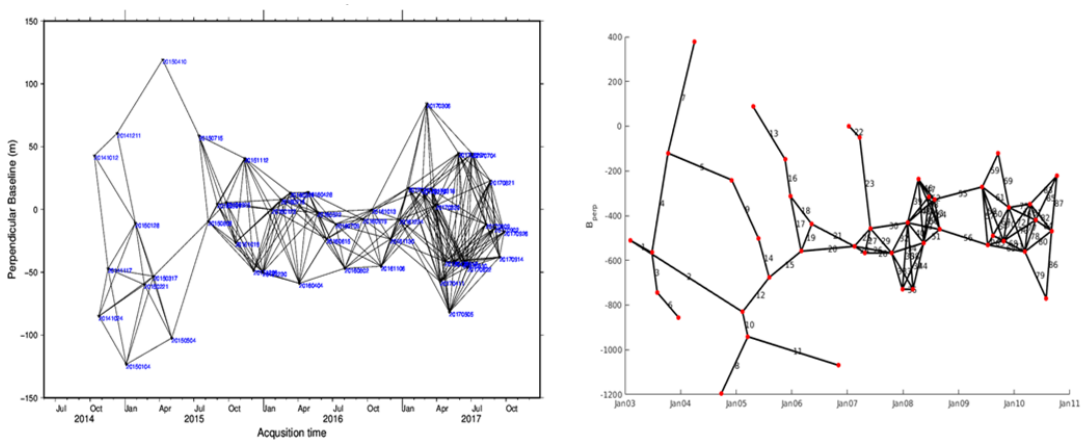

Fig. 6: Small baseline pairs from 50 images Sentinel-1A Ascending in Ciloto, Indonesia (left) and 44 images Envisat Descending in Baja California, Mexico (right).

Tab. 1: InSAR processing Parameters on StaMPS for both study areas

Parameter	Value		Parameter	Value	
	Mexico	Indonesia		Mexico	Indonesia
DEM (SRTM)	30 m	30 m	SCN time win	365	365
Max DEM error	5	5	Merge resample size	100	0
Filter grid size	50	50	Unwrap grid size	200	200
CLAP α	1	1	Unwrap time win	730	730
Spatial density rand	2	2	Unwrap goldstein filter	0.8	0.8

2.4 Power law Tropospheric Delay Correction

The power law method accounts variations spatially and temporally at tropospheric properties and belongs to phase-based tropospheric delays. It corrects only stratified delay and turbulent mixing still remains. How to reduce the effect of turbulent mixing will be explained at Section 3. The interferometric tropospheric phase $\Delta\phi_{tropo}$ could be estimated using the relationship between the interferometric phase and the topography described by BEKAERT, 2015 as

$$\Delta\varphi_{tropo} = K'_{\Delta\varphi}(h_o - h)^{\alpha}, with\ h < ho \tag{6}$$

where $K'_{\Delta\phi}$ = coefficient relating phase to topography with spatial and temporal variation, h_o = the power law reference height, α = power law coefficient. α is an empirically constant calculated from balloon sounding data provided by International Upper Air network data, the Department of Atmospheric Science of the University of Wyoming. We used WIII Jakarta Station (106.65° ; -6.11° ; Number 96749) approximately 78 km away from Ciloto, Indonesia and NKX Sand Diego Station (-117.12° ; 32.85° ; Number 72293) approximately 130 km away from Baja California, Mexico. These sounding measurements provide atmospheric properties, such as, pressure, temperature, relative humidity and wind speed, to calculate the refractivity (equation 1), tropospheric delay (equation 2 & 3) hence the relative tropospheric delay with $\Delta d_{tropo} = d_{tropo}(t_{master}) - d_{tropo}(t_{slave})$.

The power law exponent α could be found from the slope of linear fit by plotting log-log relationship between the mean tropospheric delay d_{tropo} and relative height (h_o-h). h_o is being set to the altitude with estimating no relative delays ($\Delta d_{tropo} \approx 0$) between acquisitions as illustrated on Figure 7. Furthermore, $K'_{\Delta\phi}$ is estimated in local windows using band-filtered phase according to the pixel values between the interferometric filter phase $\Delta\phi_{filt}$ and the power law scaled heights $(h_o\text{-}h)^{\alpha}$. We set the parameter of power law spatial band to 1000 - 1100 m in Ciloto and 4000 – 12000 m in Ensenada assuming the suitable-fit band filters excluding the deformation signal on those areas. The number of windows for local estimation depends on the size area. We set 50 windows with overlap 50% in Baja California case and 2 windows with overlap 10% in Ciloto case because the small location does not have extremely „varying“ topography at certain lengths.

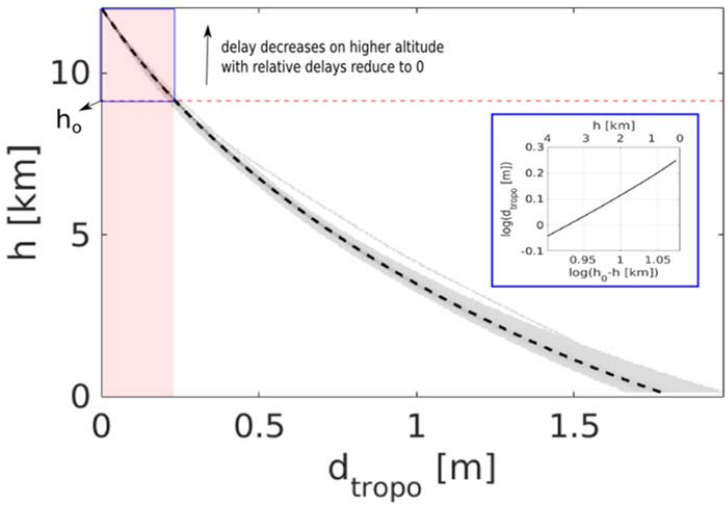

Fig. 7: Tropospheric delay in Northern Baja California, Mexico computed from upper-air sounding data at San Diego Station, 72293 located ~ 130 km away from the observed study area with the blue rectange line described as log-log relationship indicating power law relationship as we assume a linear model. The red colour shows the interferometric delay at this reference height is approximately zero and will be neglected in the tropospheric correction.

3 Result and Discussion

3.1 Corrected interferograms with power law method in Ciloto, Indonesia

SAR images from Sentinel-1A ascending orbit have been processed and generated 269 interferograms. We drop out 19 interferograms for further time series computation since the residuals between small baseline (SB) network and inverted to single master (SM) network are more than 2π in magnitude indicating unwrapping problem (HOOPER et al. 2008). The phase unwrapped continue to be processed on the Toolbox for Reducing Atmospheric InSAR Noise (TRAIN) created by BEKAERT (2015) with power law method fully implemented.

Phase tropo delay based on power law method has been computed on 250 interferograms. The success of applying this method is depending on a relationship between phase and topography assuming APS dominant by stratified delay so that it will be appropriate to power law function. We compare some interferograms which has high and low correlations between phase and elevation. Figure 8a shows an example of interferogram (20150317 – 20150808, ifg 24) where the stratified delay clearly appears on phase unwrapped result. Nevertheless, an interferogram (20141211 – 20150128, ifg 13) does not have a good correlation to topography terrain as shown on Figure 8c. The graphic at the bottom right refers to the power law method not successful for mitigating the phase delay. Moreover, this correction could make the final phase interferogram having another bias than the original interferogram. Overcoming the problem that might be appears in some interferograms, we smooth the corrected phase in time series analysis by low-pass filtering in which we predict the bias as spatially correlated noise due to either turbulent mixing or phase unwrapped error.

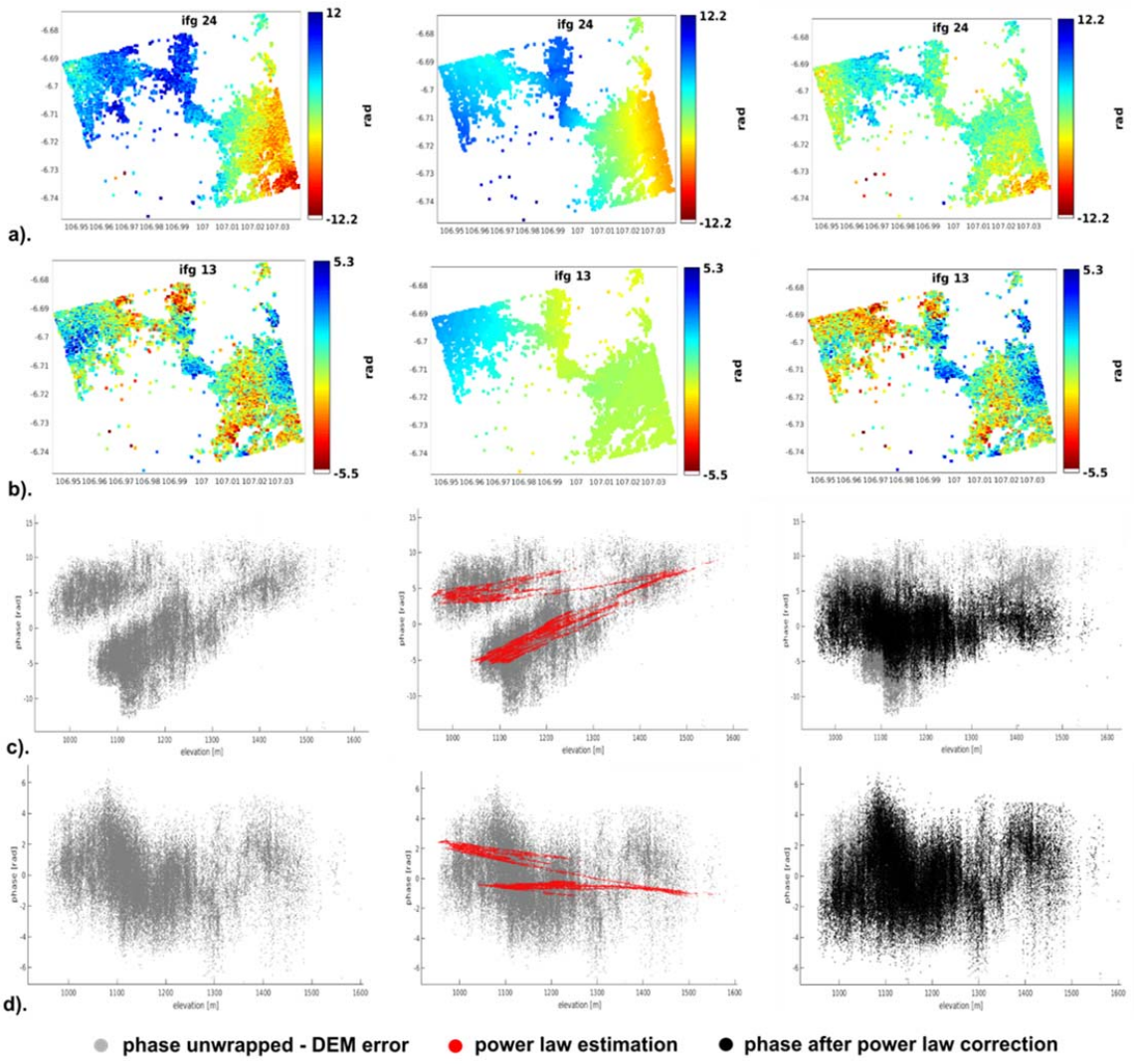

Fig. 8: The left images are original phase unwrapped including DEM error correction, the middles are estimation of power law phase delay and the rights are the corrected phase after power law correction. (a) and (b) refer to sample of success and unsuccessful corrected interferograms with (c) and (d) showing the relationship between phase and topographic height in Ciloto, Indonesia.

3.2 Time series displacement and assessment in Ciloto, Indonesia

250 interferograms with SB network will be inverted using least square to SM network (Schmidt, 2003) in purpose to calculate the time series displacement and mean velocity each PS pixels. The final interferometric phase $\Delta\phi_{depo}$ is PS scatters after substraction from DEM error (δ_{topo}), phase ramp (δ_{orbit}), stratified tropospheric delay ($\delta_{tropo,strat}$) and spatial correlated noise ($\delta_{corr.noise}$), which is described as

$$\Delta\varphi_{defo} = \Delta\varphi - \delta_{topo} - \delta_{orbit} - \delta_{tropo,strat} - \delta_{corr.noise} \quad (7)$$

The mean velocity computed by the general least-squares from October 2014 – September 2017 in Ciloto could be seen on Figure 9. It is calculated with an assumption that the displacement on

every range SAR acquisitions is a linear regression model. Moreover, it accounts only for a depiction of Ciloto's surface change for 3 years aiming to a visualization of PS scatters. It considers that -10 – +10 mm/year slow rate displacement occurs in Ciloto. There are a few PS scatters having high deformation signals in the middle of the case study where the previous geological research (SUMARYONO et al. 2015) described the location as an active landslide zone. It is also near to Puncak highway Km. 81 which in 2015 and 2017 small scale landslides occurred at the area. However, PS results cannot detect clearly the movement's behavior due to limitation of SAR resolution and lack of the exist-able for high correlated pixels.

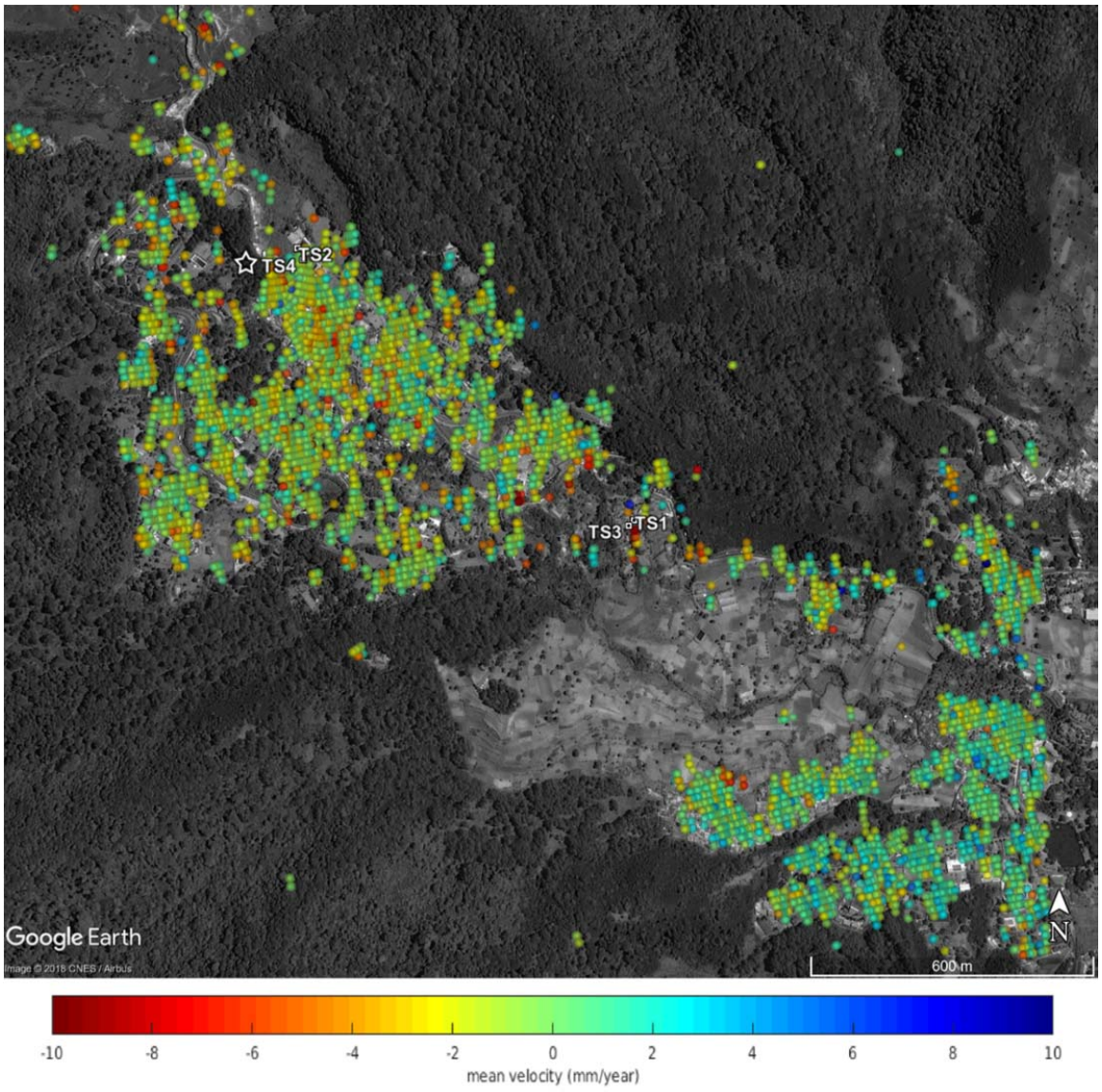

Fig. 9: The mean velocity of slope movement -10 – +10 mm/year in Ciloto landslide prone area. The type of movement is considered as a slow rate displacement with the high signal deformation is found in the middle of study area. TS2, TS4 are a sample of time series displacement near to Extensometer location (the star symbol). TS1, TS3 are located to main body of Landslide Ciloto which recent years a few active landslide occurred.

Viewing on the main body of prone landslide zone, sample points TS1, TS3 have detected ground movement -4.3 mm/year and -1.96 mm/year, respectively. TS1 refers to a sample for regular InSAR processing and TS3 after corrected tropospheric phase delay. Figure 10 shows PS scatters found on radius 25 m from TS1, TS3. There are only a few scatters left on the area since it was difficult to find persistent objects on agricultural area. Simply a linear model to figure out the mean velocity has been conducted using ordinary least square method described as

$$disp_{TS1} = -0.0207t - 3.8072 \pm 0.31$$
$$disp_{TS3} = -0.0223t - 5.7450 \pm 0.39$$

The mean velocity of TS1 and TS2 are -7.5437 ± 2.22 and -8.1615 ± 2.79 mm/year. The model exaggerates the average time series values 0.0087 and 0.0169 /day accumulating to 3.2051 and 6.1959 /year.

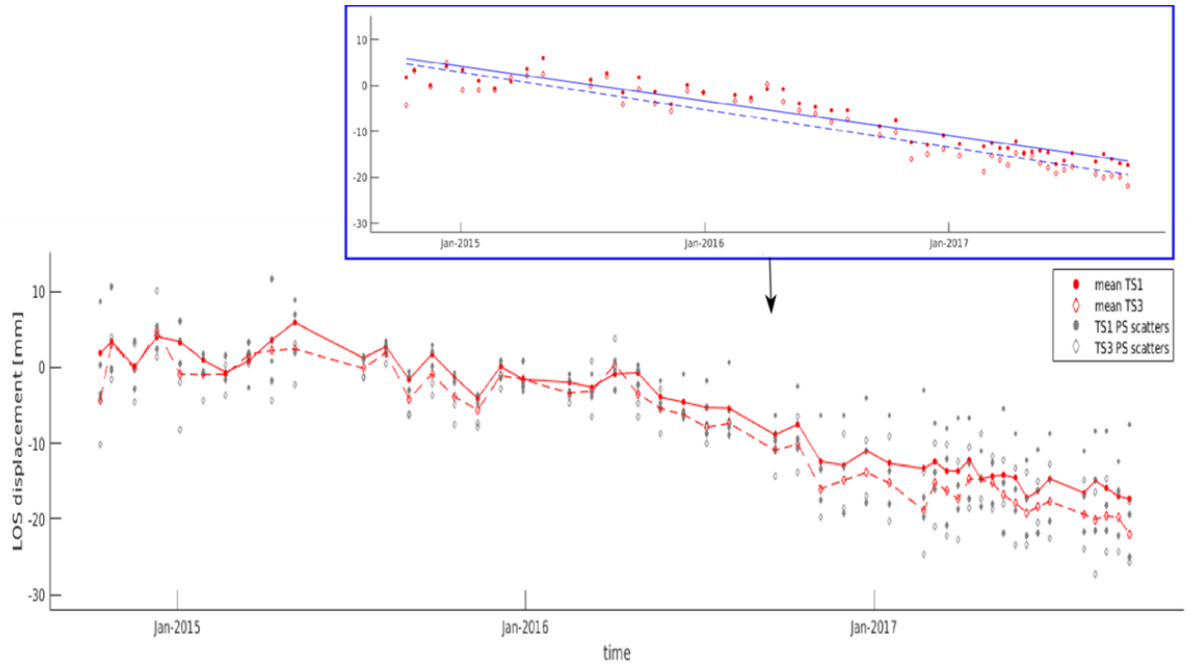

Fig. 10: Time series displacements of TS1, TS3 points (107.0021° E, -6.7119° S) located on Jl. Raya Puncak Km. 81, Ciloto. The blue box indicates the linear model movements both from InSAR results before (solid blue line) and after power law correction (dash blue line).

Furthermore, the result of InSAR processing series need to be compared to ground measurement installed on the study area to quantify before and after corrected tropospheric delay. *Balai Penyelidikan dan Mitigasi Bencana Geologi* (BPPTKG), The Ministry of Energy and Mineral Resources of the Republic of Indonesia has built 3G Track Extensometer, Cipanas Station, located at Kampung Puncak RT06/01 Desa Ciloto, 106°59"41.90" E and 6°42' 26.3" S. The real-time updates of recorded extensometer could be browsed online via BPPTKG's official website (*http://www.merapi.bgl.esdm.go.id/gertan/grafik.php?ids=28*). They installed rain gauge sensor also at the station but unfortunately it was not working thus there are no recorded data from rainfall intensity.

We divide the time of extensometer to be two part based on the reference height of displacement in raw data due to re-installment of the wire. The displacement trend from a first part is corrected to the trend showed on Figure 11a because of an assumption having systematical error + 0.14 cm. Since the verified raw data need to be discussed with BPPTKG directly, we only assess the correlation from second part in which we do not find any systematical error, presuming the wire working properly. TS2, regular InSAR processing, and TS4, corrected tropospheric phase delay InSAR processing, are located at 106.9959° E, -6.707° S. The mean time series displacements for 28 scatters of 50 m around the center could be seen on Figure 11a with ± 50 m the spatial length difference between PS scatters and the extensometer location. Figure 11b indicates a correlation between extensometer and InSAR result before and after troposphere phase delay. It uses linear Pearson's correlation using a Student's *t* distribution for the correlation's transformation to quantify the measurements. The correlation value before tropospheric delay is 0.7674 and after 0.8125. There is a small better accuracy after power law correction, in other words, it increases 0.0451.

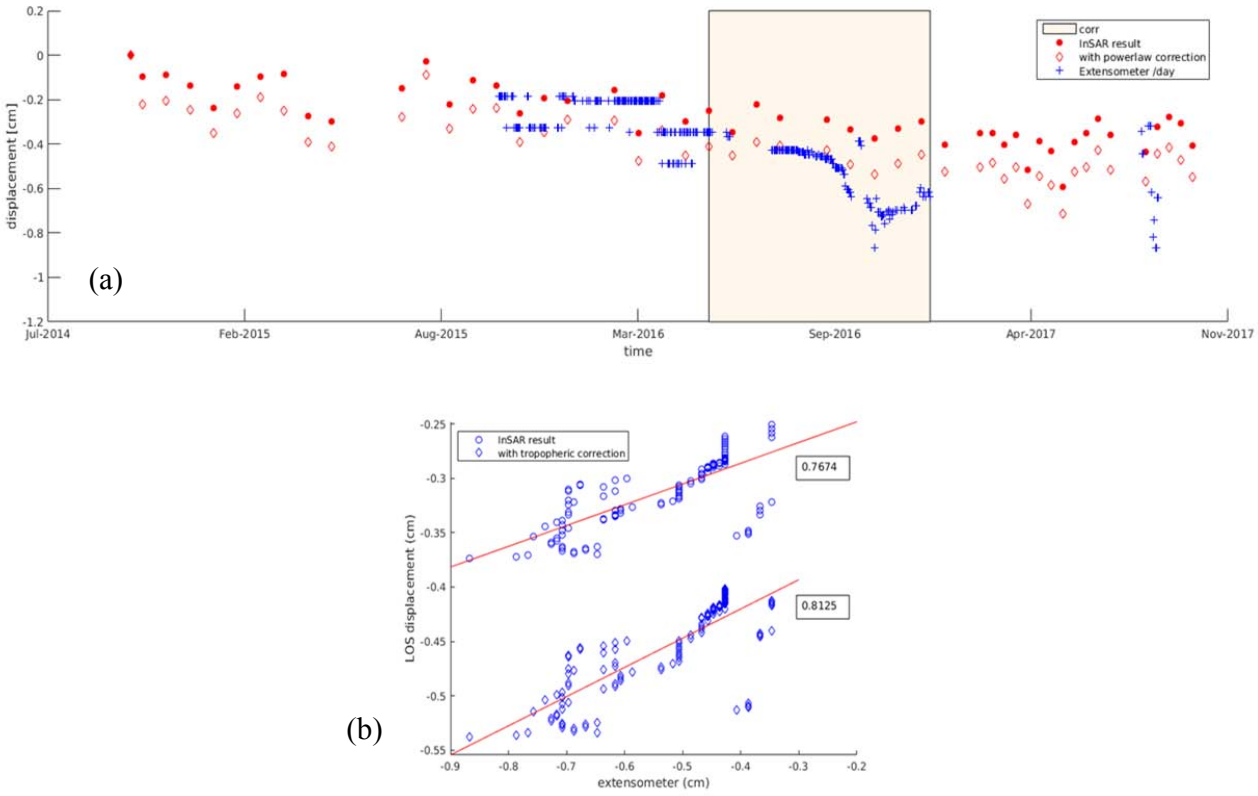

Fig. 11: (a) Time series LOS displacement samples from TS2 point (before power law correction) and TS4 point (after power law correction) compare to extensometer displacement (local geometry). (b) A correlation between extensometer and LOS displacement from 22 May 2016 to 02 Jan 2017 (a corr. rectangle box).

3.3 Corrected interferograms with power law method in Northern Baja California, Mexico

SAR images from Envisat descending orbit has been processed and generated 87 interferograms. As previous case, we correct the tropospheric delay for each interferogram. The terrain in Northern Baja California mostly mountainous area with the flat terrain found near to the coast. The stratified delay is more dominant causing atmospheric phase screen than turbulent mixing due to the varying topographic range and the demonstration of propagating delay from ERA-1 data. An example from an interferogram (18^{th} Nov 2015 – 23^{rd} Dec 2005 with B⊥ -165m) having a high atmospheric artifact could be seen on Figure 12a. The high correlation accounts

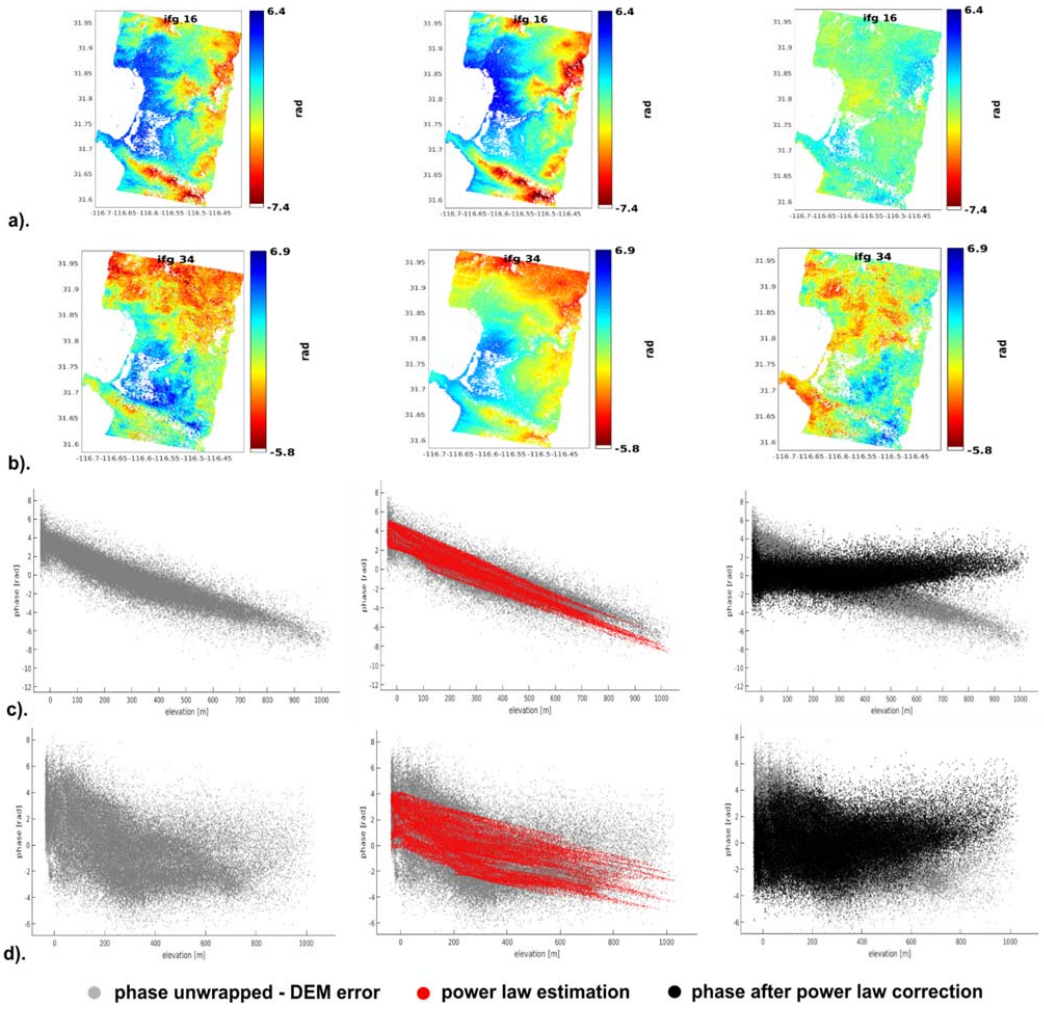

Fig. 12: The left images are original phase unwrapped including DEM error correction, the middles are estimation of power law phase delay and the rights are the corrected phase after power law correction. (a) and (c) refer to sample of success and unsuccessful corrected interferograms with (b) and (d) showing the relationship between phase and topographic height in Northern Baja California, Mexico.

the power law function mitigating the propagation effect properly. Nonetheless, a problem may appear if a region is effected by either subsidence or uplift correlated to topography. Hence, it makes the deformation signal accidentally filter out as well. This is a drawback that we should concern besides paying attention as well for choosing a right band filtering to estimate reliable coefficients $K'_{\Delta\phi}$.

Not all interferograms are properly working to a power law function, some interferograms may have a partial success tropospheric correction or unsuccessful whether phase delay is fully not correlated to topography or the band filter is chosen incorrectly. One solution deciding the right band filter is trying some windows size and compares the result to weather model or non-deformed regions. The bandwith is limited to the spatial extent of the study area for the largest window size and to the resolution of resample size for the smallest one (BEKAERT et al. 2015). We have tried 4 power law spatial bands, 2000 – 8000; 4000 – 10000; 4000 - 12000; 4000 – 14000 m, and selected [4000 12000] m as briefly discussed on section 2.4 with a reason that most estimated tropospheric delays have scale range value similar to original interferograms. Figure 12c refers to a corrected interferogram (19 Oct 2007 – 16 May 2008 with B⊥ 45 m) partially mitigating the propagating delay. Moreover, the left Figure 12c declares clearly that the power law method had an over-estimation phase delay creating a strong artifact in La Bufadora and Punta Banda regions (southwest from the study area).

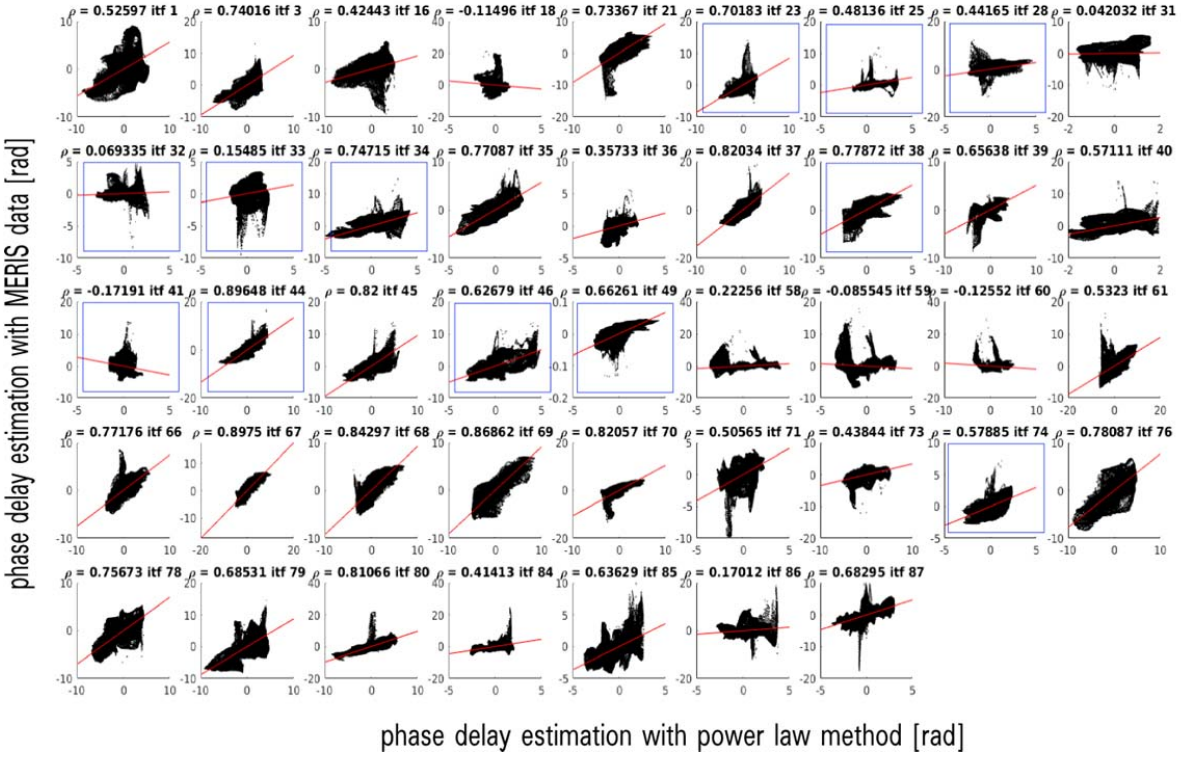

Fig. 13: The correlation of estimated phase delay between phase based - power law and spectrometer - MERIS method with 50% threshold of free cloud coverage while the blue line box refers to 90% threshold of it.

We statistically compared the power law method to MERIS computation. Because ASAR and this spectrometer instrument are operated on the same on-board Envisat Satellite, there is no time delay to estimate an atmospheric delay for each SAR acquisition. However, the drawback to use MERIS data is the daily varying cloud coverage. It makes the success of estimation depending on how much free cloud exist at Mexico region. We have tested 50% and 90% threshold free cloud coverage with the result 29 and 14 out of 44 SAR images, respectively. The mean correlation value between the phase based power law and spectrometer MERIS is 0.52 for 50% threshold and 0.53 for 90% threshold with the fitted number of interferograms showed on Figure 13.

If we consider 15 interferograms from 90% threshold as the appropriate comparison to quantify power law method, 10 out of 15 have a high correlation (mean corr = 0.7) while interferograms 25,28,32,33 and 41 show a low correlation (mean corr = 0.2). In spite of an inaccurate a surface interpolation for the gaps fill of cloud mask, the different correlation values are caused by the type of source delay estimated from spectrometer and phase-based method. The MERIS correction is generated an estimation coming from a wet delay which includes stratify and turbulent components. On the other hand, a phase-based estimation is only from a stratified component but combining hydrostatic and wet delay. A hydrostatic component could be added to MERIS result using the weather model, such as, ERA-1 data. However, the mean correlation after adding the hydrostatic term from ERA-1 does not increase significantly (0.52 for 50% threshold) since a low coarse resolution (~80 km) of ERA1-1 limits the varying hydrostatic delay in spatial. Another reason supposes that some interferograms do not have a high impact from the stratified delay examined by 5 low correlated interferograms. Their correlation to the height terrain encourage the point of view that only interferogram 33 has a high correlation (corr = 0.79) with the other rest numbers 25,28,32,41 showing low correlation -0.44, 0.54, 0.11, -0.58, respectively. Namely, the influence could be from either a turbulent component, dynamic local weather, or unknown noise errors could occur at some acquisition dates.

3.4 Time series displacement and assessment in Northern Baja California, Mexico

The northern part of the Peninsula of Baja California (Mexico), south of Ensenada at the Pacific Ocean has mountain ranges up to 1000 m and arable land in the valleys. The morphology in those areas created some environmental issues either due to concessive natural or human activities. The Agua Blanca fault strikes from northwest to southeast and is a right-lateral strike-slip fault, which was reactivated during the development of the San Andreas Fault. Moreover, the excessive use of groundwater for agricultural, urban, commercial and touristic infrastructure put a big pressure on the aquifers with loss of groundwater supply and quality. Therefore, an investigation needs to be conducted in purpose to support the technical decision policy.

For the first observation, we seek a long-term fault slip along Agua Blanca fault using InSAR time series from Envisat descending data during 8 years. The propagating delay could mask out the sensitivity of InSAR performance for detecting the real signal of deformation, especially for the case of Agua Blanca fault surrounded by mountainous terrain with the most extreme height difference of 1 km. The mean velocity using a general least-squares method and Envisat oscillator correction (MARINKOVIC et al. 2015) has been generated to overview surface's changes

which there are significant artifacts clearly showed by a conventional InSAR SB network on Figure 14a. Although inversion SM (Fig. 14b) network has been done to reduce the noise, it still appears at the southeast observed area. Therefore, on the following paragraphs, we examine the result of corrected tropospheric delay time series (TS) InSAR (Fig. 14c) categorized in three groups. The first group explains a few TS points (TS1; TS2; TS3) along Agua Blanca fault to infer a slip rate

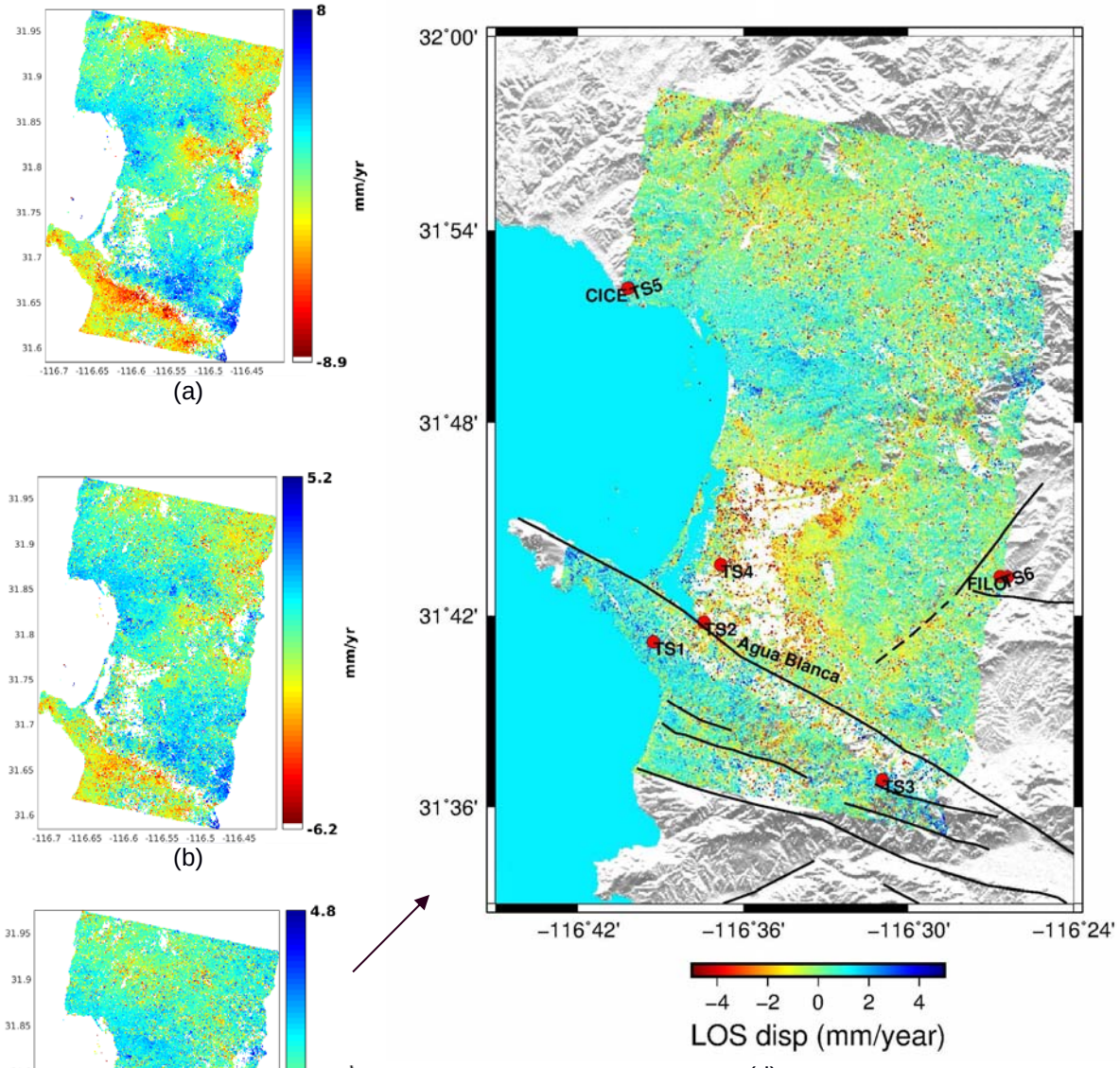

Fig. 14: (a) The mean velocity generated from (a) conventional time series InSAR SB network, (b) with inversion to SM network and (c) after tropospheric delay has been corrected using power law method. (d) The mean velocity for final InSAR results overlaying on SRTM with sample time series points located at Agua Blanca strike-slip fault, Maneadero and GPS locations.

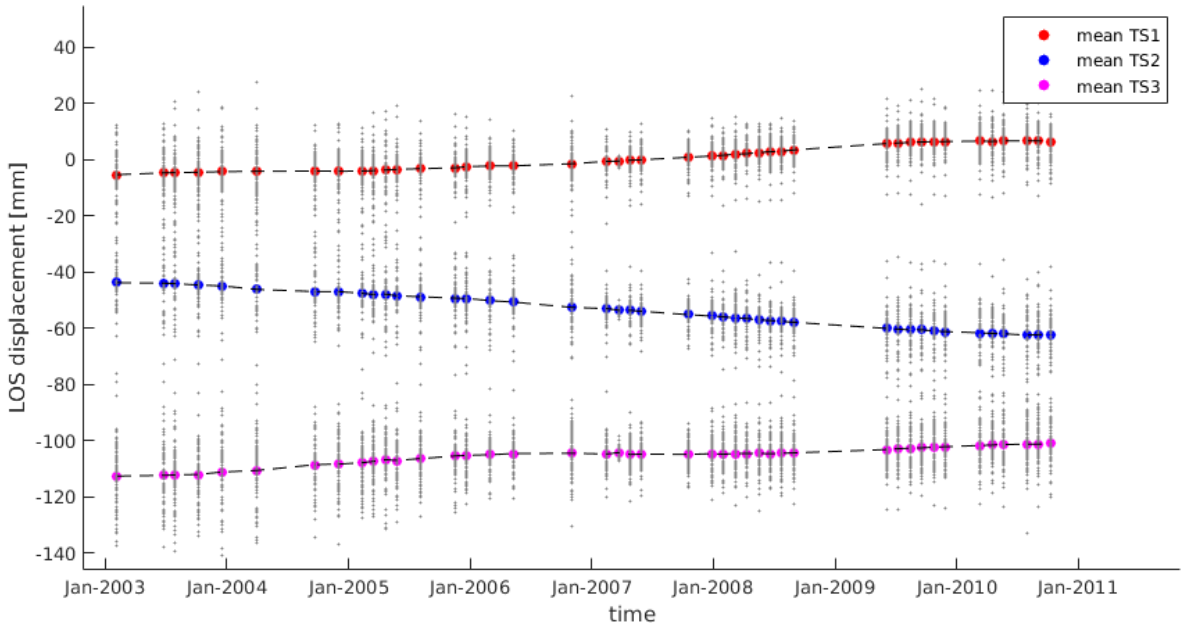

Fig. 15: Time series displacement TS1 (-116.6546°, 31.6862°), TS2 (-116.6239°, 31.6964°), TS3 (-116.5158°, 31.6141°). The average movement is calculated from PS scatters found in radius of 500 m from each point. The Figure has been shifted in y axis aiming for display.

displacement. The second one (TS4) is exploring Manaedero Valley where an environment issue arrised recent years due to over-exploitation water pumping. The last group (TS5; TS6) is a general resemblance between two TS points and GPS points (CICE, FILO) located on the covered area.

According to Figure 15, the mean velocity of TS1, TS2, TS using linear model as written on Section 3.2 are 1.832 ±0.87, -2.688 ±0.43, 1.34 ±1.02 mm/year and considered as a slow rate motion. DIXON et al. 2000 suggested that the fault is active but seismically quiet. There is a similar uplift pattern between TS1 & TS3 that might assume the points placed on „tectonic block“. These results are agree to the previous conducted research from ANIKA et al. 2018 which described the southern part of Aqua Blanca fault laid on the same block and having a similar movement behavior. Although the range TS1 and TS3 is approximately 15 km away agree to a major right lateral strike-slip (ALLAN et al. 1960), we cannot determine whether it is a total offset along the fault because we miss the horizontal components, noise scatters are existing in the middle of Agua Blanca fault and some parts have been masked out due to high decorrelation. On the other hand, TS2 acts differently to TS1, TS3 where the area found depressed or down lift to -2.688 mm/year. Moreover, not only verification to this behavior motion needs to be compared to ground observation but also a geometry relationship between the ground and LOS direction is highly recommended in the future.

We further investigate in general Maneadero Valley where the region has been actively exploited for groundwater to support the agriculture liveliness. Unfortunately, there is not enough PS scatters left on the middle of region due to a decorrelated characteristic for vegetation cover. Near to the coastal dunes, the mean velocity of InSAR reveals that the surface's level around San

Miguel decreases to -2.41 ± 0.76 mm/year using a linear approach of time series displacement for 8 years showed as Figure 16. The graphic presents a down lift movement which is likely occurred because of soil degradation. Wind and water highly contributes to the erosion in fact that ecologically the area belongs to a sand spit landform modified by agriculture and urban areas (MARTINEZ et al. 2007). Since it is salt marshes located close enough to the shoreline, the motion easily gets influence by wind-driven currents, tidal currents, wave action and seasonal weather especially during winter. Regarding to the assumption of sinking land level at a developing salt marsh, there should be an area with the rate of sediment build up (RAFFERTY 2011) and it is seen at southwest from San Miguel (TS4 mark) which PS scatters showing an uplift movement. In addition, the InSAR results are not significantly detecting any subsidence signal in Maneadero City. Hence, we consider the region is more stable sustained by the geological structure of volcanic and sediment rocks than Manaedero Valley with the alluvial material structure.

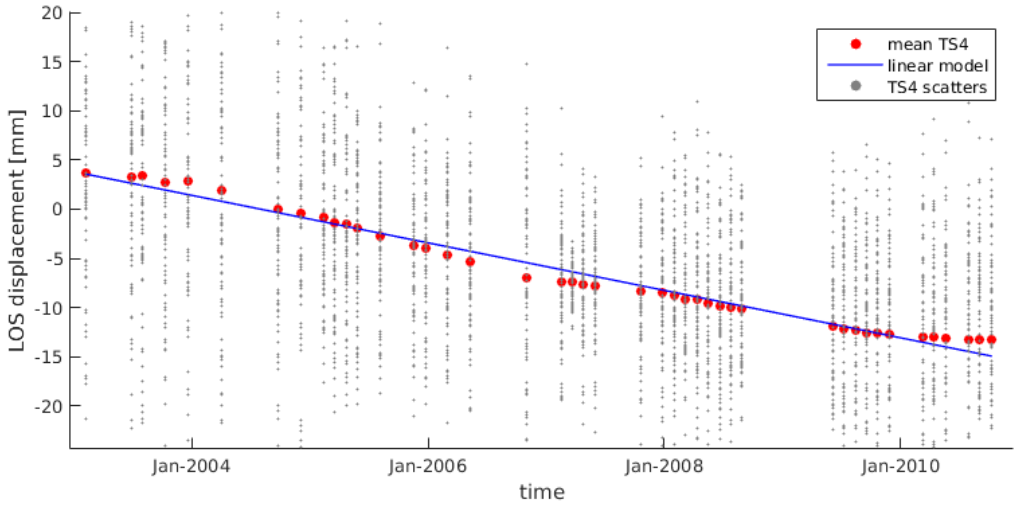

Fig. 16: Time series displacement TS4 (-116.6137°, 31.7264°) located around San Miguel, Baja California. The mean movement is calculated from 81 PS scatters found at radius 500 m from the centre. The level is sinking likely due to soil degradation.

Based on the previous research using GPS observation from 1993 to 1998 (Dixon et al, 2002), the mean velocity is about 5 mm/year across the Agua Blanca and San Miguel Vallecitos faults. Our location only covers the small part of a whole long-term slip rate area across these two faults. Therefore, we only discuss two GPS points, CICE, northwestern direction, and FILO, western direction, at northern Baja California. The sample of TS5 and TS6 represents to GPS locations where 69 and 59 PS scatters found in radius 500 m from the center of TS5 and TS6. We focus only to the vertical components generated from GPS because of unavailability the horizontal component from InSAR results. Since we processed only the descending orbit, the slant range is more sensitive to vertical and west-east than north-south direction. The condition is hardly possible to retrieve the full displacement vector (d_z, d_e, d_n) even if we use both ascending and descending interferograms. The velocities generated both by GPS relative to ITRF-96 from 1993 to 1998 and SBAS InSAR from 2003 to 2011 could be seen on table 2. We projected the LOS displacement to a vertical component using the look angle information on selected PS

pixels. Furthermore, the mean vertical velocity of InSAR results are calculated based on weighted least squares – linear line fit.

Tab. 2: GPS velocities relative to ITRF-96 for CICE and FILO station (Source: DIXON et al. 2002) and InSAR velocities samples for TS5 and TS6 points generated by 44 Envisat descending images.

Point	Latitude	Longitude	Velocity (mm/year)			Duration
			North	East	Vertical	
CICE	31.87°	-116.67°	17.5 ± 0.6	-38.0 ± 0.9	1.5 ± 2.0	1993 - 1998
TS5	31.87°	-116.67°	-	-	0.91 ± 1.8	2003 - 2011
FILO	31.72°	-116.44°	17.3 ± 1.1	-39.5 ± 1.7	1.4 ± 3.2	1993 - 1998
TS6	31.72°	-116.44°	-	-	-0.47 ± 0.6	2003 - 2011

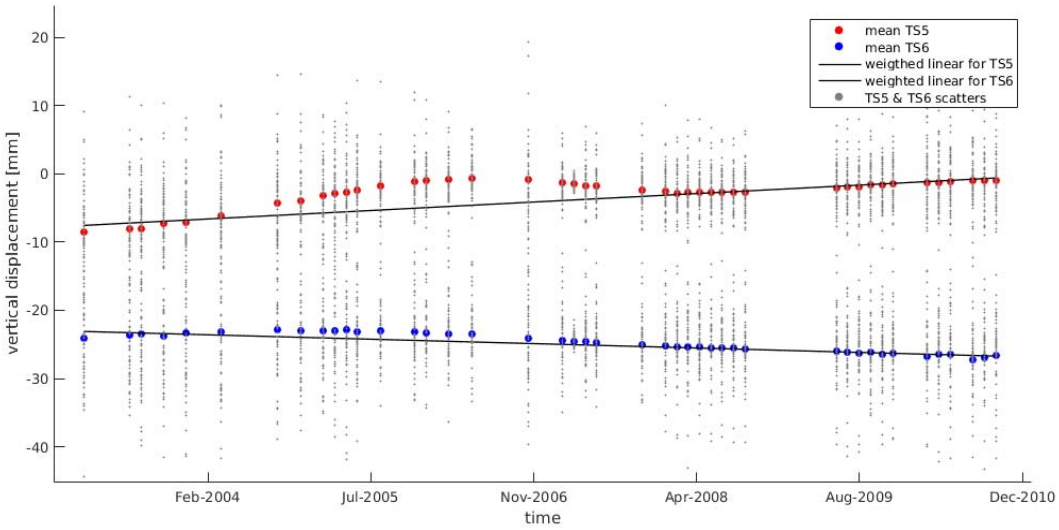

Fig. 17: Time series displacement TS5 (-116.67°, 31.877°) and TS6 (-116.44°, 31.72°) located at CICE and FILO marks from GPS observation. The means are calculated from 69 and 59 PS scatters found at radius 500 m from the centers. The Figure has been shifted in y axis aiming for display.

CICE station has same behavior to TS5 considering that the area was moving up 1.5 ± 2.0 and 0.91 ± 1.8 mm/year. Nevertheless, TS6 acted differently to the movement recorded at FILO station. The FILO records showed uplift to 1.4 ± 3.2 on the contrary TS6 down lift to -0.47 ± 0.6 mm/year. There are a few reason that the vertical components between GPS and InSAR projected results acted differently. In point of geometric reason, GPS is the most insensitive measurement to the vertical component otherwise the slant-range of SAR has the most insensitivity decomposition to north-south component. Hence in fact, the fault belongs to strike-slip type which horizontal displacements are more taking into account than the vertical one. According to the processing strategies, a few concerns are firstly that the band-filter process in

tropospheric delay correction could accidentally remove a deformation signal because of the parallel movement direction to terrain. Secondly, the unsuccessful corrected tropospheric delay and a random noise might still remain. Moreover, FILO station was located at steep terrain which retrieving the side-looking displacement is a challenge due to geometric distortions in the SAR image.

4 Conclusion

We conducted the performance of power law method to mitigate the tropospheric delay over Ciloto, Indonesia and Baja California, Mexico. The correction allows estimating locally varying interferometric phase delay signal in spatial. We tested the method on mountainous terrains at small and large areas. Although the validation to the ground measurement, the extensometer, showed an increased correlation before and after tropospheric delay correction, the performing is way better to be applied at large area in condition to the dominant delay's source from a stratified term. The reason is the spatial scales over these areas change significantly in pressure, temperature and relative humidity. However, the power law method is only successful when the cases have relative delays appropriate to power law function. If it is not, it might introduce incorrect signals because of under or over tropospheric signal estimation subjecting to turbulent variations and local weather. A further tropospheric mitigation needs to use the combination method of phase-based, spectrometer and weather model phenomena with developing an optimization algorithm to select the most accurate strategy being applied to each interferogram.
The quality of slow rate displacement time series InSAR could be improved with stratified tropospheric delay correction. It removes the sampling biases of time series because the stratified delay is systematically presenting seasonal fluctuations and correlated to topography. Especially for the Mexico study area, the hydrostatic delay has to be taken into account when there is more than 10 °C different surface temperature in a year (DOIN et al. 2009). Nevertheless, the displacement's value remains still in slant-range direction which in the next step of our work, we will perform both satellite's orbits for the Ciloto study area and assess the displacement's geometry projected from LOS to the ground surface direction.

5 Acknowledgement

The authors would like to thank European Space Agency (ESA) for providing the Envisat data with Proposal ID 31690 and Copernicus for open-access Sentinel-1 data. This research is funded by Deutsche Akademischer Austauschdienst (DAAD) with Research Grants 91565966. A few images are created by Generic Mapping Tools (GMT).

6 Reference

FUNNING, G.J., PARSONS, B. & WRIGHT, T.J., 2005: Surface Displacements and Source Parameters of the 2003 Bam (Iran) Earthquake from Envisat Advanced Synthetic Aperture Radar Imagery, Journal of Geophysical Research, **110**, B09406.

CHEN, M., TOMAS, R., LI, Z., MOTAGH, M., LI, T., HU, L., GONG, H., LI, X., YU, J. & GONG, X., 2016: Imaging Land Subsidence Induced by Groundwater Extraction in Beijing (China) using Satellite Radar Interferometry, MDPI: Journal of Remote Sensing, **8**, 468.

LIU, P., LI, Q., LI, Z., HOEY, T., LIU, Y. & WANG, C., 2015: Land Subsidence over Oilfields in the Yellow River Delta, MDPI: Journal of Remote Sensing, **7**, 1540-1564.

CASCINI, L., FORNARO, G. & PEDUTO, D., 2010: Advanced Low- and Full-resolution DinSAR Map Generation for Slow-moving Landslide Analysis at Different Scales. Elsevier: Journal of Engineering Geology., **112**, 29-42.

HOOPER, A., SEGALL, P. & ZEBKER, H., 2007: Persistent Scatter Interferometric Synthetic Aperture Radar for Crustal Deformation Analysis with Application to Volcán Alcedo, Galápagos, Journal of Geophysical Research, **112**, B07407.

FERRETTI, A., PRATI, C. & ROCCA. F., 2001: Permanent Scatterers in SAR Interferometry, IEEE Trans. Geosci. Remote Sens., **39** (1), 8-20.

BERARDINO, P., FORNARO, G., LANARI, R. & SANSOSTI, E., 2002: A New Algorithm for Surface Deformation Monitoring Based on Small Baseline Differential SAR Interferograms, IEEE Trans. Geosci. Remote Sens., **40**(11), 2375-2383.

DOIN, M.-P., LASSERRE, C., PELTZER, G., CAVALIE, O. & DOUBRE, C., 2009: Corrections of Stratified Tropospheric Delays in SAR Interferometry: Validation with Global Atmospheric Models, Elsevier: Journal of Applied Geophysics, **69**, 35-50.

BEKAERT, D. P. S., A. HOOPER, & T. J. WRIGHT, 2015: A Spatially Variable Power Law Tropospheric Correction Technique for InSAR Data, J. Geophys. Res. Solid Earth, **120**.

GOLDSTEIN, R., 1995: Atmospheric Limitations to Repeat-track Radar Interferometry, Geophysical Research Letters, **22**(18), 2517-2520.

HANSSEN, R.F., 2001: Radar Interferometry: Data Interpretation and Error Analysis, Dordrecht. Kluwer Academic Publisher, 130-153.

MASSONET, D. & FEIGL, K.L., 1998: Radar Interferometry and Its Application to Changes in the Earth's Surface, Reviews of Geophysics, **36**(4), 441-500.

SMITH, JR. E. K. & WEINTRAUB, S., 1953: The Constants in the Equation for Atmospheric Refractive Index at Radio Frequencies, Proceeding of the I.R.E., **41**, 1035-1037.

THAYER, G.D., 1974: An Improved Equation for the Radio Refractive Index of Air, Radio Science, **9**, 803-807.

JUNG, J., KIM D.-J., PARK, S.-E., 2014: Correction of Atmospheric Phase Screen in Time Series InSAR using WRF Model for Monitoring Volcanic Activities, IEEE Trans. Geosci. Remote Sens., **52**(5), 2678-2689.

YU, C., LI, Z. & PENNA, N.T., 2018: Interferometric synthetic aperture radar atmospheric correction using a GPS-based iterative tropospheric decomposition model, Elsevier: Remote Sensing of Environment, **204**, 109-121.

LI, Z., FIELDING, E.J., CROSS, P. & PREUSKER, R., 2009: Advanced InSAR Atmospheric Correction: MERIS/MODIS Combination and Stacked Water Pavour Models, International Journal of Remote Sensing, **30**(13), 3343-3363.

FATTAHI, H. & AMELUNG, F., 2015: InSAR Bias and Uncertainty due to the Systematic and Stochastic Tropospheric Delay, Journal of Geophysical Research: Solid Earth, **120**, 8758-8773.

DIXON, T., DECAIX, J., FARINA, F., FURLONG, K., MALSERVISI, R., BENNETT, R., SUAREZ-VIDAL, F., FLETCHER, J. & LEE, J., 2002: Seismic Cycle and Rheological Effects on Estimation of Present-day Slip Rates for the Agua Blanca and San Miguel-Vallecitos Faults, Northern Baja California, Mexico, Journal of Geophysical Research, **107**(B10), 2226.

RIEDEL, A., RIEDEL, B., SCHÖTMÜLLER, C., NIEMEIER, W. & GERKE, M., 2018: Bestimmung der Erdoberflächenbewegung mittels Radarinterferometrie nahe der Agua Blanca Störung, Baja California. Publikationen der Deutschen Gesellschaft für Photogrammetrie, Fernerkundung und Geoinformation e.V., Band 27.

SANDWELL, D., MELLORS, R., TONG, X., WEI, M. & WESSEL, P. 2011: Open Radar Interferometry Software for Mapping Surface Deformation, Eos Trans. AGU, **92**(28).

KAMPES, B., HANSSEN, R. & PERSKI, Z., 2003: Radar Interferometry with Public Domain Tools. Proceedings Fringe 2003, **6**.

HOOPER, A., BEKAERT, D., SPAANS, K. & ARIKAN, M., 2012: Recent Advances in SAR Interferometry Time Series Analysis for Measuring Crustal Deformation, Elsevier: Tectonophysics, 514-517, 1-13.

MARINKOVIC, P. & LARSEN, Y., 2015: On Resolving the Local Oscillator Drift Induced Phase Ramps in ASAR and ERS1/2 Interferometric Data - The Final Solution, in: Fringe 2015 workshop (ESA SP-731).

BEKAERT, D.P.S., WALTERS, R.J., WRIGHT, T.J., HOOPER, A.J. & PARKER, D.J., 2015: Statistical Comparison of InSAR Tropospheric Correction Techniques, Elsevier: Remote Sensing of Environment, **170**, 40-47.

HOOPER, A., 2008: A Multi-temporal InSAR Method Incorporating both Persistent Scatterer ans Small Baseline Approaches, Geophysical Research Letters, **35**, L16302.

SUMARYONO., SULAIMAN, C., TRIANA, D.Y., ROBIANA, R. & IRAWAN, W., 2015: Landslide Investigation and Monitoring at Ciloto, West Java, Indonesia, Engineering Geology for Society and Territory, **2**, 1089-1096.

MARTINEZ, M.L. & PSUTY, N.P., 2007: Coastal Dunes: Ecology and Conservation. Ecological Studies, **171**, Springer Berlin Heidelberg, 301-308.

ALLAN, C. R., SILVER, L. & STEHLI, F. G., 1960: Agua Blanca fault, A Major Transverse Structure of Northern Baja California, Mexico, Geol. Soc. Am. Bull., **71**, 457-482.

RAFFERTY, J.P., 2011: The Living Earth: Lakes and Wetlands. New York, N.Y.: Britannica Educational Publishing, Chapter 5, 132-156.